




# Heterostructured nickel–cobalt metal alloy and metal oxide nanoparticles as a polysulfide mediator for stable lithium–sulfur full batteries with lean electrolyte

Hyeona Park<sup>1</sup> | Suyeong Lee<sup>2</sup> | Hyerim Kim<sup>1</sup> | Hyunyoung Park<sup>3</sup> |  
Hun Kim<sup>1</sup> | Jongsoon Kim<sup>3,4</sup>  | Marco Agostini<sup>5</sup> | Yang-Kook Sun<sup>1,6</sup>  |  
Jang-Yeon Hwang<sup>1,6</sup> 

<sup>1</sup>Department of Energy Engineering, Hanyang University, Seoul, Republic of Korea

<sup>2</sup>LG Energy Solution, Ltd, CTO, LG Science Park, Seoul, Republic of Korea

<sup>3</sup>Department of Energy Science, Sungkyunkwan University, Suwon, Republic of Korea

<sup>4</sup>SKKU Institute of Energy Science and Technology (SIEST), Sungkyunkwan University, Suwon, Republic of Korea

<sup>5</sup>Dipartimento di Chimica e Tecnologia del Farmaco, Università di Roma La Sapienza, Roma, Italy

<sup>6</sup>Department of Battery Engineering, Hanyang University, Seoul, Republic of Korea

## Correspondence

Jongsoon Kim, Department of Energy Science, Sungkyunkwan University, Suwon 16419, Republic of Korea.  
Email: [jongsoonkim@skku.edu](mailto:jongsoonkim@skku.edu)

Marco Agostini, Dipartimento di Chimica e Tecnologia del Farmaco, Università di Roma La Sapienza, P.le Aldo Moro 5, 00185 Roma, Italy.  
Email: [marco.agostini@uniroma1.it](mailto:marco.agostini@uniroma1.it)

Yang-Kook Sun and Jang-Yeon Hwang, Department of Energy Engineering, Hanyang University, Seoul 04763, Republic of Korea.  
Email: [yksun@hanyang.ac.kr](mailto:yksun@hanyang.ac.kr) and [jangyeonhw@hanyang.ac.kr](mailto:jangyeonhw@hanyang.ac.kr)

## Funding information

National Research Foundation of Korea, Grant/Award Number: 2022R1C1C1011058; Korea Institute for Advancement of Technology (KIAT), Grant/Award Number: P0012748

## Abstract

Batteries that utilize low-cost elemental sulfur and light metallic lithium as electrodes have great potential in achieving high energy density. However, building a lithium–sulfur (Li–S) full battery by controlling the electrolyte volume generally produces low practical energy because of the limited electrochemical Li–S redox. Herein, the high energy/high performance of a Li–S full battery with practical sulfur loading and minimum electrolyte volume is reported. A unique hybrid architecture configured with Ni–Co metal alloy (NiCo) and metal oxide (NiCoO<sub>2</sub>) nanoparticles heterogeneously anchored in carbon nanotube-embedded self-standing carbon matrix is fabricated as a host for sulfur. This work demonstrates the considerable improvement that the hybrid structure's high conductivity and satisfactory porosity promote the transport of electrons and lithium ions in Li–S batteries. Through experimental and theoretical validations, the function of NiCo and NiCoO<sub>2</sub> nanoparticles as an efficient polysulfide mediator is established. These particles afford polysulfide anchoring and catalytic sites for Li–S redox reaction, thus improving the redox conversion reversibility. Even at high sulfur loading, the nanostructured Ni–Co metal alloy and metal oxide enable to have stable cycling performance under lean electrolyte conditions both in half-cell and full-cell batteries using a graphite anode.

Hyeona Park, Suyeong Lee, and Hyerim Kim contributed equally to this study.

This is an open access article under the terms of the [Creative Commons Attribution](https://creativecommons.org/licenses/by/4.0/) License, which permits use, distribution and reproduction in any medium, provided the original work is properly cited.

© 2024 The Authors. *Carbon Energy* published by Wenzhou University and John Wiley & Sons Australia, Ltd.

## KEYWORDS

full cell, high energy, lean electrolyte, Li-S batteries, polysulfide mediator

## 1 | INTRODUCTION

Reducing gas emissions and overcoming the consequent climate crisis are among the foremost problems that confront humanity in the next 50 years.<sup>1</sup> Presently, the major sources of gas emissions are industries and road transportation, which mainly rely on fossil fuels. The current strategies of companies are aimed at constantly reducing the use of fossil fuels until they can be fully replaced with sustainable resources, such as biofuels and natural gas, in the near future.<sup>2</sup> Despite being a sustainable choice, road transportation is also looking to improve the use of both hybrid and full electric vehicles to compensate for the wide demand of the market.<sup>3</sup> However, at present, the extensive use of electric vehicles is mainly hindered by the exorbitant cost of the battery pack powering these vehicles.<sup>4,5</sup> Understandably, this is because the electric vehicle battery consists of expensive elements, which are scarce in the earth's crust.<sup>6</sup> Accordingly, in the previous decade, researchers have begun to formulate new chemistries that are suitable for Li-ion technologies.<sup>7,8</sup> Among these, the technique based on lithium-sulfur (Li-S) reaction was found to have considerable potential considering the cost, availability, and theoretical energy density of sulfur.<sup>9,10</sup> The Li-S reaction mechanism has a theoretical capacity of 1675 mAh g<sup>-1</sup> with an average working potential of 2.2 V.<sup>11,12</sup> However, this reaction also introduces problems that can limit the lifecycle and practical uses of Li-S cells,<sup>13</sup> such as sulfur's low electronic conductivity and dissolution into the electrolyte, forming LiS<sub>n</sub> (1 < n < 8) polysulfide species (LiPs) that facilitate move and precipitate on the Li anode side as Li<sub>2</sub>S<sub>2</sub> and Li<sub>2</sub>S.<sup>14-17</sup> It is necessary to mitigate the sluggish sulfur conversion reactions and the shuttle effect during cycling.<sup>14-17</sup> Many papers have proposed that the synthesis of sulfur composite electrodes can possibly resolve the above problems.<sup>18-20</sup> Despite these successes, the design of electrodes based on integrating sulfur into a porous conductive network (mainly carbon) does not consider the practical capacity and energy density that the electrode can deliver.<sup>21,22</sup> The amount of electrolyte required to ensure a satisfactory electrochemical reaction is normally 8-10 times the amount of sulfur-active material in terms of weight.<sup>23</sup> This is attributed to the presence of large voids between the carbon host and sulfur particles, the presence of a considerable amount of inactive materials, and the confinement of a substantial quantity of active materials within the host.<sup>23</sup> Thus, to ensure electrode wettability and lithium diffusion into the electrodes, the electrolyte volume must be large.<sup>4,24</sup> A possible approach to reduce the required volume is to deposit sulfur directly on the conductive and

self-standing networks to assist in the redox reaction.<sup>25</sup> Of particular interest are conductive carbon nanofibers (CNFs) with a small surface area and free volume that can enable the deposition of active materials.<sup>26,27</sup> The hydrophobic surface of CNFs can also be modified using polar groups to improve interactions with soluble LiPs.<sup>28,29</sup> Owing to their high strength and excellent electrical conductivity, transition metal (TM) alloy nanoparticles have been widely investigated in electrochemical catalysts for improving electron transfer kinetics.<sup>30-33</sup> In addition, transition metal oxides with high polar surfaces were introduced for scavenging the soluble LiPs.<sup>34,35</sup> They can be directly integrated into the host structure, therefore improving the binding energy between sulfur and its host as well as enhancing the electron transfer pathways of typical "2Li + S → Li<sub>2</sub>S" conversion reaction in the electrochemical process.<sup>36-41</sup>

Inspired by previous findings, in this study, nanostructured Ni-Co metal alloy and metal oxide particles in carbon nanotubes (CNTs)/CNFs (CNTs/CNFs/Ni-Co) structures are integrated as sulfur host; the particles are implemented directly in the fiber structure during synthesis, while sulfur-active material is, subsequently, deposited on top of the CNFs host surface through a simple drop-casting procedure. Both Ni-Co metal alloy and metal oxide were selected due to their superior function for enhancing the redox conversion reversibility of Li-S cells. The reaction mechanism was investigated through combined electrochemical texts and X-ray photoelectron spectroscopy (XPS) measurements, as well as density functional theory (DFT) calculations. By taking the unique physicochemical functionalities, the sulfur-deposited CNTs/CNFs/Ni-Co electrodes can be cycled under lean electrolyte conditions (i.e., 3:1 electrolyte-to-sulfur [E/S] weight ratios) even in a Li-S full battery configuration using a lithiated-graphite anode.

## 2 | EXPERIMENTAL SECTION

### 2.1 | Synthesis of NiCo and NiCoO<sub>2</sub> embedded within porous CNF composite structure

Polyacrylonitrile (PAN, Mw = 150,000; Sigma-Aldrich) and polystyrene (PS, Mw = 192,000; Sigma-Aldrich) were dispersed in *N,N*-dimethylformamide (DMF; Sigma-Aldrich) in a 1:1 ratio corresponding to 20 wt.% of the solution. The following were added to this solution: 0.8-mmol nickel(II) acetate tetrahydrate (NiAc<sub>2</sub>; Sigma-Aldrich), 0.8-mmol cobalt(II) acetate tetrahydrate (CoAc<sub>2</sub>;

Sigma-Aldrich), and CNTs corresponding to 10 wt.% of PAN. Then the mixture was stirred overnight at 70°C. The CNTs/CNFs/Ni-Co composite was obtained using the electrospinning method. To fabricate the composite structure, the solution described above was fed into a syringe and then electrospun at 16 kV with a spinning distance of 10 cm and a feeding rate of 20  $\mu\text{L min}^{-1}$  using a 21-gauge needle tip; the rotational speed was 450 rpm. The composite structure was stabilized in air at 200°C for 1 h and carbonized at 1000°C for 2 h with  $\text{N}_2$  flow. The structure thickness varies from 250 to 300  $\mu\text{m}$ . For comparison, the composite structures were also synthesized at carbonization temperatures of 700°C and 1100°C. In addition, the porous CNF composite structure (CNTs/CNFs) was synthesized using the same process without the Ni and Co acetate tetrahydrate solution.

## 2.2 | Synthesis of sulfur CNTs/CNFs/Ni-Co and sulfur CNTs/CNFs cathodes

To introduce sulfur to the CNTs/CNFs/Ni-Co and pristine CNTs/CNFs, a 1-M solution of  $\text{Li}_2\text{S}_8$  DME was deposited by drop casting. The solution was prepared by dissolving 1 mol of  $\text{Li}_2\text{S}$  and 7 mol of S in 1 L of 1,2-dimethoxyethane (DME) solution at 60°C and stirred until the solution turned red. After cutting into the 9.5-mm (0.708  $\text{cm}^2$ ) diameter composite structure disk, the solution was directly dropped on the top of both electrodes. The electrodes were heated at 80°C for 10 min to completely evaporate the DME solvent. The sulfur loading on CNTs/CNFs/Ni-Co and pristine CNTs/CNFs corresponded to the solution amount.

## 2.3 | Material characterizations

The crystalline phases of the prepared materials were characterized by powder XRD (PAN analytical, Empyrean) with Cu-K $\alpha$  radiation. The morphologies and elemental distributions of the prepared materials and samples cross-sectioned by focused ion beam milling were observed by scanning electron microscopy (SEM) (JEOL JSM 6400) and transmission electron spectroscopy (TEM) (JEOL 2010). The electronic conductivity was measured by the direct volt-ampere method (CMT-SR1000) where a disk sample was brought into contact with a four-point probe; TGA was performed with a thermal analysis instrument (STA 449C, Netzsch) with  $\text{N}_2$  flow at a heating rate of 10°C  $\text{min}^{-1}$ . The polysulfide adsorbability levels of CNTs/CNFs/Ni-Co and pristine CNTs/CNFs were measured by UV/vis spectroscopy (V-670; JASCO) after dispersing 10 mg of CNTs/CNFs/Ni-Co in 2 mL of 0.0025-M  $\text{Li}_2\text{S}_8$  DME. The specific

surface area, pore size, and volume were measured using a Brunauer-Emmett-Teller analyzer (Quantachrom Autosorb-1 equipment). The samples were also analyzed using XPS (PHI5000 Versaprobe) to measure the binding energy. During this measurement, the sample was packaged and transferred into a vacuum to preclude exposure to moisture and air.

## 2.4 | Electrochemical measurements

For the half-cell tests, the sulfur CNTs/CNFs/Ni-Co and sulfur pristine CNTs/CNFs cathodes were punched into 0.95-cm diameter disk (0.708  $\text{cm}^2$  in area). These were directly used as working electrodes with the Li metal as counter and reference electrodes. The average  $\text{Li}_2\text{S}_8$  loads in the CNTs/CNFs/Ni-Co electrodes were approximately 4 and 7  $\text{mg cm}^{-2}$ . The electrolyte was a combination of 0.8-M  $\text{LiNO}_3$  and 0.5-M lithium bis(trifluoromethanesulfonyl) imide (LiTFSI) dissolved in a 1:1 (volume/volume) mixture of 1,3-dioxolane (DOL) and 1,2-dimethoxyethane (DME). The half-cells were fabricated with electrolytes using E/S of 10, 5, and 3. The polymer membrane (Celgard 2400) was used to separate the electrodes. The half-cells were prepared in an Ar-filled dry box (MBRAUN) and cycled in the voltage range of 1.8–2.6 V at 25°C. For the full-cell assembly based on the sulfur CNTs/CNFs/Ni-Co cathode and graphite anode, the sulfur loading in the cathode was 3  $\text{mg cm}^{-2}$ . The full-cell balance was achieved by limiting the capacity ratio to 1.2:1 (anode:cathode) Graphite (POSCO Chem, Inc.) was mixed with carbon black (Super P; TIMCAL) and water-based polyacrylic acid binder at a mass ratio of 95:2.5:2.5. The slurry was coated on the Cu foil and dried at 100°C for 24 h in a vacuum oven. Before the cell assembly, the anodes were cycled three times between 0.01 and 3.0 V at a current rate of 0.1 C (1 C = 375  $\text{mAh g}^{-1}$ ) with Li metal as the counter electrode; the electrolyte was a combination of 2.5-M LiTFSI and 0.4-M  $\text{LiNO}_3$  in DME:DOL (1:1 by volume). The full cells were fabricated with electrolytes using E/S of 10, 5, and 3. The full cells were prepared in an Ar-filled dry box and cycled in the voltage range of 1.0–2.6 V at 25°C. The current rates for all cycling and/or C-rate tests referred to the theoretical capacity of sulfur (1675  $\text{mAh g}^{-1}$ ). The specific capacities were calculated based on the sulfur mass loadings.

## 2.5 | First-principles calculations

All the DFT calculations were performed using the Vienna Ab initio Simulation Package (VASP).<sup>42</sup> Projector-augmented wave pseudopotentials were used with a plane-wave basis set, as implemented in VASP.<sup>43</sup>

Perdew–Burke–Ernzerhof (PBE) parametrization of the generalized gradient approximation (GGA)<sup>44</sup> was used. For DFT calculations, a  $2 \times 2 \times 1$  k-point grid was used to calculate each surface structure. The GGA + U<sup>32</sup> method was adopted to address the localization of the d-orbital in Ni and Co ions, with  $U_{\text{eff}}$  values of 5.5 and 6.6 eV, respectively, as used in the previous studies.<sup>45,46</sup> For the more accurate calculation results for van der Waals interaction between lithium polysulfide and substrate, the DFT-D3 correction method<sup>47</sup> was considered in this study. A kinetic energy cutoff of 500 eV was used in all the calculations, and all the structures were optimized until the force in the unit cell converged within  $0.03 \text{ eV } \text{Å}^{-1}$ .

In this study, structural data for NiCo and NiCoO<sub>2</sub> were obtained from the Inorganic Crystal Structure Database (ICSD). After the relaxation process to optimize the DFT calculation, each structure was cleaved along the (110) plane for NiCo and (100) plane for NiCoO<sub>2</sub>, to generate the surface model.

The adsorption energy ( $E_{\text{ads}}$ ) derived from the following equation:

$$E_{\text{ads}} = E_{\text{surface@Li-S}} - (E_{\text{surface}} + E_{\text{Li-S}}),$$

where  $E_{\text{surface@Li-S}}$  is the total energy of substrate which adsorbed lithium polysulfide molecule,  $E_{\text{surface}}$  is the total energy of the pristine substrate, and  $E_{\text{Li-S}}$  is the total energy of lithium polysulfide molecule.

### 3 | RESULTS AND DISCUSSIONS

#### 3.1 | Synthesis and characterization of CNTs/CNFs/Ni-Co

The Ni-Co metal alloy (NiCo) and metal oxide (NiCoO<sub>2</sub>) anchored to the CNTs-embedded porous CNFs composite was synthesized via the electrospinning method. The synthesis details are shown in the schematic in Figure 1A and discussed in the experimental section. After the heat treatment at 1000°C for 2 h under N<sub>2</sub> gas flow, flexible and freestanding CNTs/CNFs/Ni-Co (Figure 1B,C) with an average thickness range of 200–250 μm (SEM image of cross-section, Figure 1D) is derived. The SEM images of CNTs/CNFs/Ni-Co show that the nanofibers have a three-dimensional porous structure with randomly dispersed smooth fibers with diameters in the range of 1–1.5 μm (Figure 1E,F). Note that multiple pores in CNFs can be

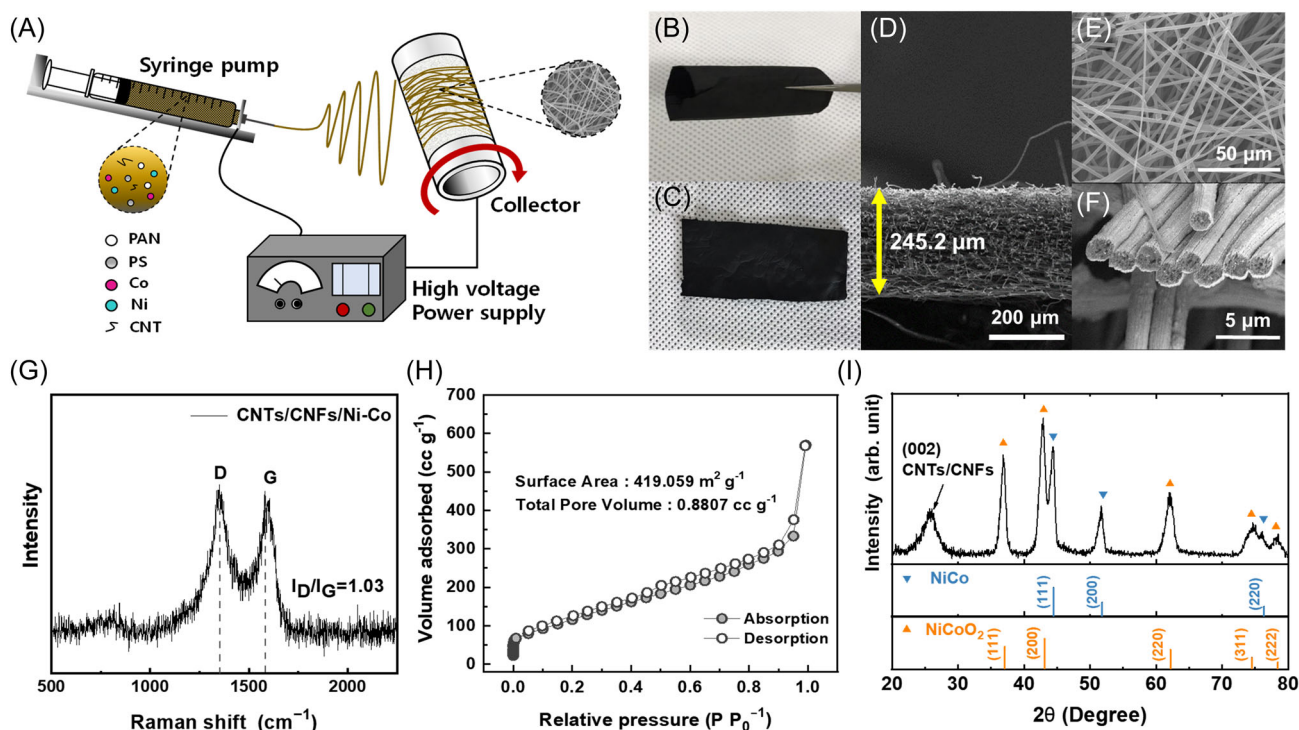


**FIGURE 1** Schematic synthesis and characterization of CNTs/CNFs/Ni-Co: (A) schematic synthesis of CNTs/CNFs/Ni-Co through electrospinning (21-gauge syringe needle; flow rate:  $20 \mu\text{L min}^{-1}$ ) and (B, C) digital photographs of flexible and self-standing CNTs/CNFs/Ni-Co. (D) Cross-sectional SEM image, (E) pristine SEM image, (F) focused ion beam (FIB)-SEM image of CNTs/CNFs/Ni-Co nanofiber, (G) Raman spectrum, (H) nitrogen adsorption–desorption isotherms, and (I) XRD pattern. The inset of (H) shows the corresponding surface area and total pore volume.

formed through the decomposition of polystyrene and thus elasticity may be increased by decreasing mechanical toughness and stress.<sup>48</sup> Raman spectroscopy analyses (Figures 1G and S1) show that the CNTs/CNFs/Ni-Co has a relatively ordered graphitic carbon structure based on a relatively low I(D)-I(G) intensity ratio of ~1.03. The results of the nitrogen adsorption and desorption tests (Figure 1H) conducted on CNTs/CNFs/Ni-Co indicate the surface area and cumulative pore volume to be 419.06 m<sup>2</sup> g<sup>-1</sup> and 0.88 cm<sup>3</sup> g<sup>-1</sup>, respectively, with mesopore and micropore distributions (Figure S2). The X-ray diffraction (XRD) pattern (Figure 1I) shows the heterogeneously co-existence of NiCo and NiCoO<sub>2</sub> phases in the carbon fiber matrix.<sup>49,50</sup> Through investigation of different heat treatment temperatures, it was found that the crystallinity of the nanoparticles was not sufficient at 700°C, and intense peaks corresponding to metal due to excessive reduction were shown at 1100°C, confirming that the heat treatment at 1000°C was the best temperature (Figure S3).

To better understand the presence of NiCo and NiCoO<sub>2</sub> in CNTs/CNFs/Ni-Co, XPS (Figure 2A,B) analysis was performed. The Ni 2p spectra clearly show distinguishable peaks at 854.4 and 872 eV assigned to the Ni<sup>2+</sup>, and peaks at 852.95 and 870 eV assigned to metallic Ni<sup>0</sup>.<sup>48-52</sup> The Co 2p spectra show peaks at 780 and 795 eV assigned to Co<sup>2+</sup>, and peaks at 778 and 793 eV assigned to metallic Co<sup>0</sup>.<sup>49-52</sup> The results further prove the co-existence of NiCo and NiCoO<sub>2</sub> in the CNTs/CNFs/Ni-Co.<sup>50,53</sup> The N 1s spectra (Figure S4) also confirmed the small level of nitrogen doping of the carbon structure induced by the decomposition of the nitrile group in

polyacrylonitrile (PAN) during synthesis.<sup>54,55</sup> The scanning transmission electron spectroscopy (STEM) and high-resolution TEM images show that the CNTs and pores are uniformly dispersed inside the fibers (Figure 2C,D). To further investigate the structural and chemical properties of the material used, the selected CNTs/CNFs/Ni-Co samples were cross-sectioned using a focused-ion beam and analyzed using STEM (Figure 2E). The high-resolution transmission electron microscopy (HR-TEM) images of the white circles (Figure 2E) confirm the lattice fringes of NiCo alloy and NiCoO<sub>2</sub>, demonstrating their coexistence (Figures 2F,G and S5).<sup>53-55</sup> TEM and corresponding energy dispersive X-ray spectroscopy (EDX) elemental mapping (Figure 2H-I3) indicates the unique structural features of CNTs/CNFs/Ni-Co with NiCoO<sub>2</sub> and NiCo nanoparticles webbed in the CNTs and anchored to the CNF matrix. A pristine CNTs/CNFs material was also prepared via an identical synthesis route without Ni and Co metal sources and characterized using elemental mapping by SEM (Figure S6) and TEM with EDX (Figure S7). The electrical conductivities of the pristine CNTs/CNFs and CNTs/CNFs/Ni-Co supports are calculated to be 5.5 and 0.61 S cm<sup>-1</sup>, respectively, from the equation ( $\sigma = t/R_s$ , where  $\sigma$  is the electrical conductivity of materials,  $R_s$  is the sheet resistance measured using 4-point probe equipment, and  $t$  is the thickness of the materials).<sup>56,57</sup> Note that although the metal oxides afford natural insulation, their electrical conductivity is partially compensated by the presence of CNTs and NiCo metal alloy particles.<sup>53,55</sup> Accordingly, CNTs/CNFs/Ni-Co has sufficient electrical conductivity to compensate for the

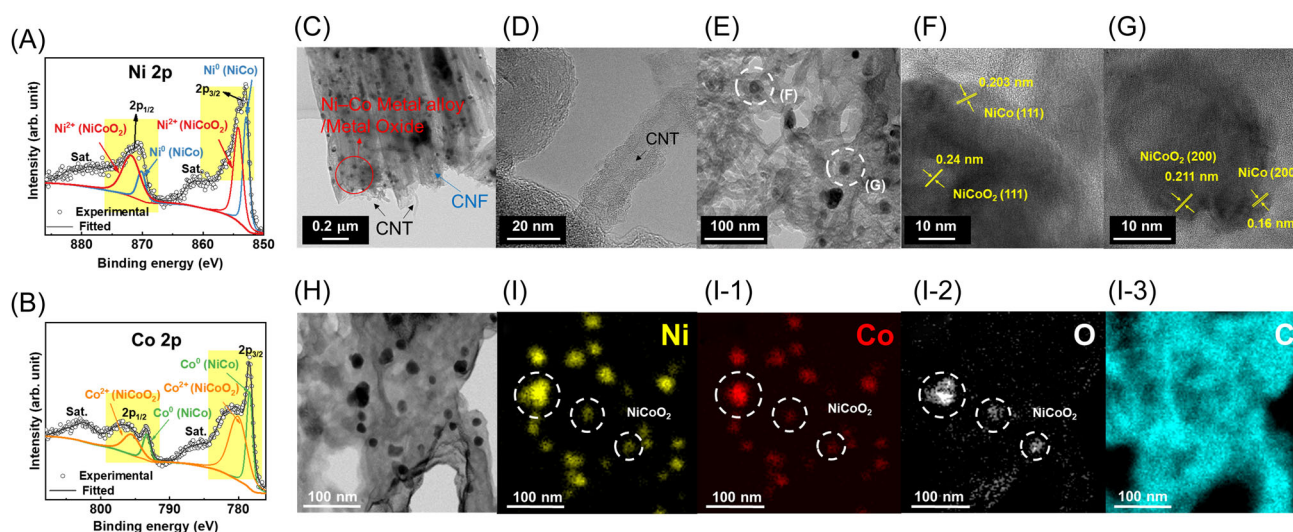


**FIGURE 2** Characterization of CNTs/CNFs/Ni-Co: XPS analysis for (A) Ni 2p and (B) Co 2p. (C) STEM image and (D) HR-TEM image for the edge region of CNTs/CNFs/Ni-Co. (E) STEM image of cross-sectioned CNTs/CNFs/Ni-Co using FIB milling and (F, G) HRTEM images of Ni-Co particles marked as a white circle in (E). (H) TEM images and (I1, I2, I3) corresponding EDX mapping of Ni (yellow), Co (red), O (white), and C (blue), respectively.

problem of sulfur's intrinsic insulating properties to host sulfur in Li-S batteries.

### 3.2 | Polysulfide trapping interfaces of Ni-Co heterogeneous metal and metal oxide

In this work, the interactions of LiPs with CNTs/CNFs/Ni-Co were investigated through combined DFT calculation, visual observation, and ultraviolet-visible (UV-vis) spectroscopy analysis (Figure S8). We used 10 mg of CNTs/CNFs/Ni-Co soaked in a solution of DME and 2.5 mM of  $\text{Li}_2\text{S}_n$  polysulfide. For qualitative comparison, the test was also performed for the pristine CNTs/CNFs material. After 30 min of immersion, the  $\text{Li}_2\text{S}_n$  solution slightly changed in color, indicating that the pristine CNTs/CNFs only weakly interacted with LiPs because only physical adsorption was involved through their pores. In contrast, the  $\text{Li}_2\text{S}_n$  solution containing CNTs/CNFs/Ni-Co became transparent after 10 min because NiCo and  $\text{NiCoO}_2$  adsorbed the polysulfide from the solution. This confirmed the occurrence of pore adsorption and strong Lewis acid-base interactions.<sup>58,59</sup> The UV-vis spectroscopy further demonstrated the strong chemical affinity of NiCo and  $\text{NiCoO}_2$  with soluble  $\text{Li}_2\text{S}_n$ . The peaks at 350, 475 nm of  $\text{S}_6^{2-}$  and 420 nm of  $\text{S}_4^{2-}$ , represented by the yellow color, virtually lost all their intensities compared with those of pristine CNTs/CNFs, confirming the better chemical adsorption of the proposed modified nanofiber network.<sup>60</sup>

First-principles calculations were performed to further understand the interaction between the NiCo and  $\text{NiCoO}_2$  surfaces by comparison with the graphene surface. The adsorption energy ( $E_{\text{ads}}$ ) for lithium sulfide ( $\text{Li}_2\text{S}_x$ ) and sulfur ( $\text{S}_8$ ) on each substrate was calculated in Figure 3A. The negative  $E_{\text{ads}}$  values indicated a strong interaction between lithium sulfide species and substrates. Compared to graphene substrates, NiCo and  $\text{NiCoO}_2$  have a stronger binding affinity to lithium polysulfides; in particular, notably, lithium polysulfide molecules are strongly bound to  $\text{NiCoO}_2$  substrate due to their polar nature.<sup>61</sup> The detailed adsorption structures of lithium polysulfides on different substrates are illustrated in Figure 3B–D. It can be suggested that the strong affinity of NiCo and  $\text{NiCoO}_2$  substrate to lithium polysulfide can help suppress the shuttling effect of lithium polysulfides during cycling. Furthermore, the theoretical Gibbs free energies for the corresponding lithium-sulfur conversion reactions on graphene, NiCo, and  $\text{NiCoO}_2$  were gained via first-principles calculation. The  $\text{Li}_2\text{S}_8/\text{Li}_2\text{S}_6$  reaction undergoes liquid-liquid transition during the reaction since  $\text{Li}_2\text{S}_8$  and  $\text{Li}_2\text{S}_6$  are soluble.

This liquid-liquid transition gives some advantages to ensure that the conversion occurs in fast kinetics.<sup>62</sup> On the other hand, the  $\text{Li}_2\text{S}_4$ -to- $\text{Li}_2\text{S}_2$  and  $\text{Li}_2\text{S}_2$ -to- $\text{Li}_2\text{S}$  conversions are the important steps to evaluate the electrochemical performance of Li-S cathode since these reactions have happened during liquid-solid and solid-solid phase transformation; moreover,  $\text{Li}_2\text{S}_2$ -to- $\text{Li}_2\text{S}$  conversion is commonly the rate-determining step on the lithium-polysulfide conversion.<sup>16,62</sup> As illustrated in Figure 3E, the conversion reaction from  $\text{S}_8$  to  $\text{Li}_2\text{S}_8$  occurs spontaneously due to the negative Gibbs free energy change in the discharge process on graphene, NiCo, and  $\text{NiCoO}_2$ . After the  $\text{S}_8$ -to- $\text{Li}_2\text{S}_8$  conversion, the Gibbs free energy gradually increased in all substrates; however, these conversion reactions are more advantageous for NiCo and  $\text{NiCoO}_2$ . Among the substrates, NiCo alloy exhibits the lowest Gibbs free energy barrier of  $\sim 1.79$  eV, indicating that the total conversion reaction of lithium sulfide species is thermodynamically more favorable. Moreover,  $\text{NiCoO}_2$  exhibits a Gibbs-free energy barrier at an appropriate level along with high adsorption energy for lithium sulfide species, supporting an efficient overall lithium-polysulfide conversion reaction. Therefore, the synergetic effect of NiCo and  $\text{NiCoO}_2$  as polysulfide mediators is better than that of graphene, which is consistent with experimental results. From the first-principles calculation, we confirmed that the proposed NiCo and  $\text{NiCoO}_2$  play an important role as polysulfide mediators with a synergistic effect in adsorbing the soluble polysulfide as well as the catalytic effect of lithium-sulfur conversion.

### 3.3 | CNTs/CNFs/Ni-Co as the polysulfide mediator

To fabricate the sulfur electrode,  $\text{Li}_2\text{S}_n$  was deposited on CNTs/CNFs/Ni-Co by drop casting 1 M of  $\text{Li}_2\text{S}_8/\text{DME}$  solution (Figure 4A). The solvent was evaporated to remove the excess weight before assembling the Li-S cell. The electrode was prepared with a sulfur mass loading of  $7.5 \text{ mg cm}^{-2}$ . The sulfur content was approximately 71.8 wt.% of the total electrode mass, as confirmed by thermogravimetric analysis (TGA) and SEM-EDX analysis (Figures 4B and S9). Note that considering the pore cumulative volume of  $0.88 \text{ cm}^3 \text{ g}^{-1}$ , CNTs/CNFs/Ni-Co can theoretically load up to 64 wt.% of sulfur ( $2.07 \text{ g cm}^{-3}$ ) into the pores.<sup>60</sup> This leads to the conclusion that most of the sulfur has actually penetrated the porous CNTs/CNFs/Ni-Co composite. Approximately 7 wt.% of sulfur is present on the electrode surface as a result of anchoring to NiCo and/or  $\text{NiCoO}_2$ . The TEM and corresponding EDX mapping data (Figure 4C–F) indicate

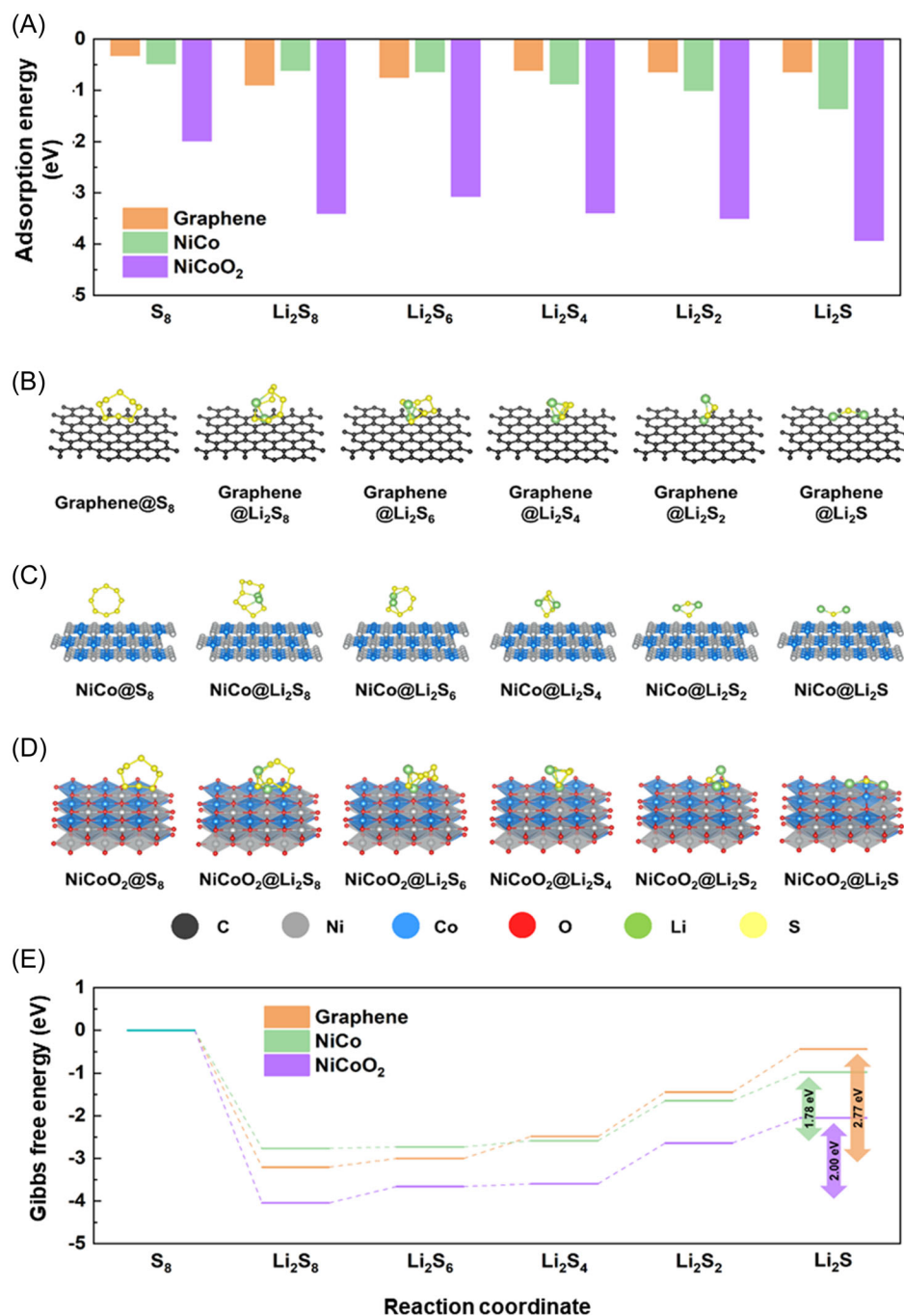


**FIGURE 3** First-principles calculation results: (A) calculated adsorption energies for lithium polysulfide ( $\text{Li}_2\text{S}_x$ ) and sulfur ( $\text{S}_8$ ) on graphene, NiCo, and NiCoO<sub>2</sub> substrate. (B–D) Optimized adsorption structure for lithium polysulfide ( $\text{Li}_2\text{S}_x$ ) and sulfur ( $\text{S}_8$ ) on graphene, NiCo, and NiCoO<sub>2</sub> substrate, respectively. (E) Gibbs free energy profile for the lithium-sulfur conversion reactions on graphene, NiCo, and NiCoO<sub>2</sub> substrate.

that sulfur is uniformly distributed in CNTs/CNFs/Ni–Co and enables the satisfactory affinity of NiCo and/or NiCoO<sub>2</sub> to sulfide species.

Note that the Li–S cells previously reported in the literature were generally fabricated under loose experimental control; in particular, a relatively large amount of electrolyte was employed. They exhibited satisfactory

capacity and cycling properties; behind those shining performances, however, their systems had inadequate applicability due to the low practical energy densities achieved. Hence, in this study, Li–S cells using the CNTs/CNFs/Ni–Co electrode with various sulfur loads (4 and 7.5 mg cm<sup>-2</sup>) and ratios of electrolyte volume to sulfur weight (E/S, in  $\mu\text{L}/\text{mg}$ ), specifically, 3, 5, and 10, were

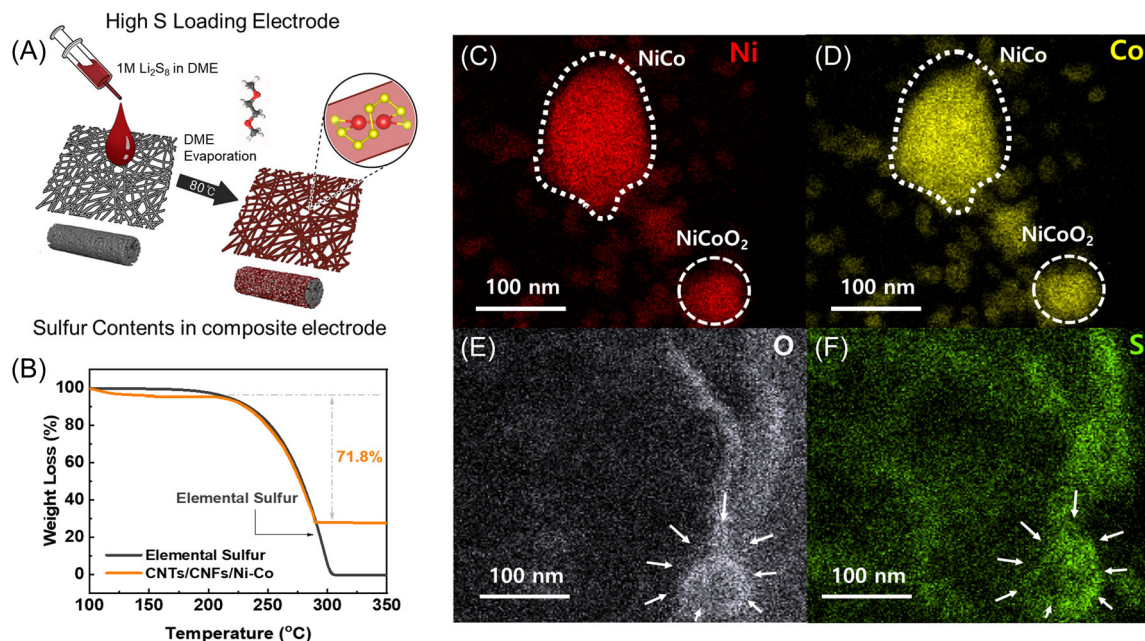


**FIGURE 4** Characteristics and trapping of lithium polysulfide in CNTs/CNFs/Ni-Co. (A) Polysulfide adsorption through solvent casting on the CNTs/CNFs/Ni-Co; (B) TGA of elemental sulfur ( $S_8$ ) and S-CNTs/CNFs/Ni-Co composite; and (C–F) EDX mapping for Ni (red), Co (yellow), O (white), and S (green), respectively.

fabricated to demonstrate superior electrochemical performance with low E/S. For comparison, the pristine CNTs/CNFs electrode was also evaluated. To confirm the electrochemical redox reactions of CNTs/CNFs/Ni-Co and pristine CNTs/CNFs electrodes in Li-S cells, cyclic voltammetry (CV) was initially conducted at a scan rate of  $0.05 \text{ mV s}^{-1}$  in the voltage range of 1.8–2.6 V (Figure 5A,B). For the first scan, both electrodes exhibited typical double-stage reduction and oxidation reactions. The two distinctive reduction peaks at 2.34 and 2.02 V are assigned to the high-order ( $\text{Li}_2\text{S}_x$ ,  $4 \leq x \leq 8$ ) and low-order ( $\text{Li}_2\text{S}_2$  and  $\text{Li}_2\text{S}$ ) reductions of sulfur during the cathodic segment, respectively. The two peaks at 2.3 and 2.41 V during the anodic segment are assigned to the reversible oxidation process.<sup>16,36</sup> In the succeeding cycles, however, the pristine CNTs/CNFs electrode compared with the CNTs/CNFs/Ni-Co electrode showed irreversible redox reactions with relatively large voltage polarization and low output current. For the cycling test, both electrodes were first activated once at low current rates of 0.1 and 0.2 C ( $1 \text{ C} = 1675 \text{ mA g}^{-1}$ ) before they were subjected to prolonged galvanostatic cycling under various test conditions. With a moderate E/S of 10 (sulfur loading of  $4.0 \text{ mg cm}^{-2}$ ) at a current rate of 0.5 C, the CNTs/CNFs/Ni-Co electrode delivered a discharge capacity of  $1276.9 \text{ mAh g}^{-1}$  higher than that yielded by the pristine CNTs/CNFs electrode ( $1159.4 \text{ mAh g}^{-1}$ ). It also had better capacity retention with higher Coulombic efficiency and no capacity loss upon cycling (more than

100 cycles) (Figure 5C,D). The effect of the presence of NiCo and NiCoO<sub>2</sub> as polysulfide mediators is more distinct under constrained test conditions (sulfur loading:  $7.5 \text{ mg cm}^{-2}$ ; E/S = 5). Hence, the reversible capacity of the pristine CNTs/CNFs electrode compared with that of the proposed electrode was two times lower. Moreover, it had a drastic capacity loss with considerably unstable Coulombic efficiency after 33 cycles (Figures 5E,F and S10). This capacity drop is attributed to the undesirable “shuttle effect” caused by the dissolution of LiPs into the electrolyte and their subsequent deposition on the Li metal surface. This accelerates the active material loss and dendritic growth of Li, eventually leading to Li-S cell failure. In contrast, the CNTs/CNFs/Ni-Co electrode demonstrated a higher discharge capacity of  $1100.2 \text{ mAh g}^{-1}$  and superior cycling stability and Coulombic efficiency after 50 cycles. These performance improvements in terms of reversible capacity, rate capability, and cycle life clearly demonstrate the beneficial presence of NiCo and NiCoO<sub>2</sub> as polysulfide mediator. It can be noted that the nanostructured NiCo and NiCoO<sub>2</sub> composite not only functions as a polysulfide scavenger but also provides mechanical integrity.<sup>63,64</sup> Consequently, the volumetric changes are suppressed by adsorbing the LiP species during the Li-S cell operation.<sup>36,63</sup> Moreover, its porous network provides sufficient active sites for electrochemical reactions and physically entraps excess LiPs.<sup>18,65</sup> This results in a synergetic effect suppressing active mass loss and mitigating the

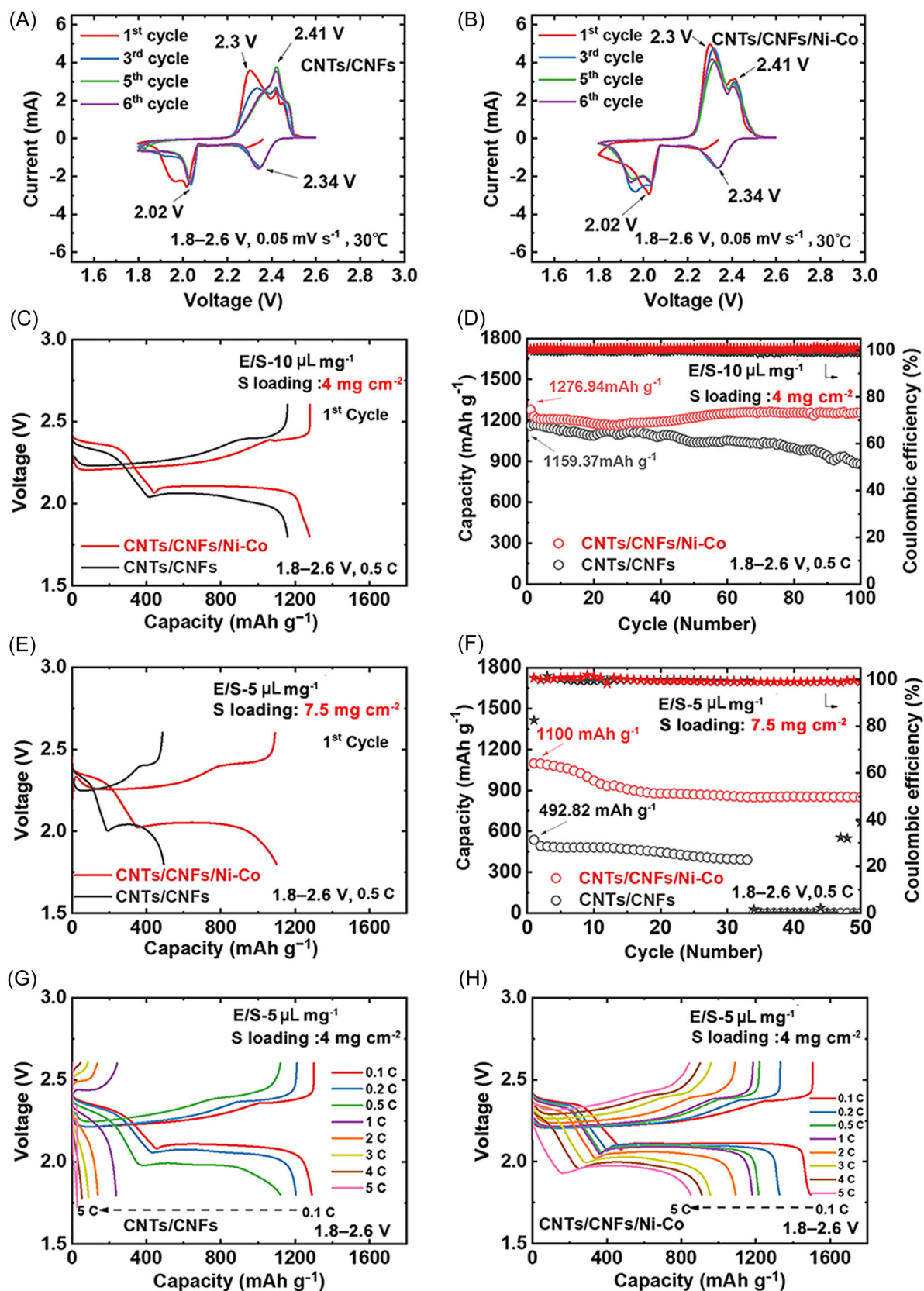


**FIGURE 5** Electrochemical performance of Li-S cells using pristine CNTs/CNFs and CNTs/CNFs/Ni-Co electrodes: (A, B) CV curves (all cells were tested in the voltage range of 1.8–2.6 V at  $0.05 \text{ mV s}^{-1}$ ), (C) voltage profiles of cells with sulfur loading of  $4 \text{ mg cm}^{-2}$  and E/S of 10 at current rate of 0.5 C, and (D) corresponding discharge capacity retention and cell efficiency during 100 cycles; (E) voltage profiles of cells with sulfur loading of  $7.5 \text{ mg cm}^{-2}$  and E/S of 5 at 0.5 C and (F) corresponding discharge capacity retention and cell efficiency during 50 cycles; (G, H) rate capability test of Li-S cells (sulfur loading of  $4 \text{ mg cm}^{-2}$  and E/S of 5) with different cell configurations. All cells were cycled at increasing current rates from 0.1 C ( $0.1675 \text{ A g}^{-1}$ ) to 5 C ( $8.375 \text{ A g}^{-1}$ ) in the voltage range of 1.8–2.6 V.

migration of LiPs to the Li metal side. The power capabilities of both pristine CNTs/CNFs and CNTs/CNFs/Ni-Co electrodes were tested at various current rates and compared under a sulfur load of  $4 \text{ mg cm}^{-2}$  and E/S of 5. The CNTs/CNFs/Ni-Co electrode showed  $852.4 \text{ mAh g}^{-1}$  of reversible capacity even at 5 C, whereas the pristine CNTs/CNFs electrode delivered inferior capacities with large voltage polarization and drastic capacity drop (Figure 5G,H). Notably, even with a high sulfur load of  $7.5 \text{ mg cm}^{-2}$  and E/S of 5, the CNTs/CNFs/Ni-Co electrode delivered  $837.05 \text{ mAh} \cdot \text{g}^{-1}$  of reversible capacity at a 2 C current rate (Figure S11). On the other hand, to confirm the synergetic effect of NiCo and NiCoO<sub>2</sub> in improving the power capability, the CNTs/CNFs/Ni-Co electrode dominated by NiCo metal alloy was synthesized by heat treatment at  $1100^\circ\text{C}$  and tested under a sulfur load of  $4 \text{ mg cm}^{-2}$  and E/S of 5 (Figure S3). Although the large fraction of NiCo metal alloy can help to improve the electronic conductivity of the electrode, the inferior reversible capacities were observed at various current rates due to the lack of LiPs adsorption ability compared with the proposed CNTs/CNFs/Ni-Co electrode (Figure S12). These improved power capabilities can be attributed to the co-existence of NiCo and NiCoO<sub>2</sub> nanoparticles, which improves the electrical conductivity as well as suppresses the loss of active mass in the electrolyte solution by trapping polysulfide in the porous structure, simultaneously. Furthermore, the well-linked CNTs/CNF network facilitates electrolyte accessibility, thereby improving Li-ion diffusion and affording better charge-transfer kinetics even under lean electrolyte condition.

### 3.4 | Postmortem analysis

The electrochemical mechanism of the CNTs/CNFs/Ni-Co electrode in Li-S cells is investigated through the postmortem analysis of the cycled cathode and Li metal anode. At the end of the discharge process (1.8 V) after 100 cycles, XPS analysis (Figure 6A,B) was performed for cycled pristine CNTs/CNFs and CNTs/CNFs/Ni-Co electrodes to investigate the chemical functionalities formed at the electrode surface. The S 2p core level in the CNTs/CNFs/Ni-Co electrode showed the main peak at 160.3 eV, which was associated with the Li<sub>2</sub>S<sub>2</sub> and Li<sub>2</sub>S species. In contrast, a relatively weak peak was observed at approximately 167.5 eV, which was ascribed to the formation of Li<sub>2</sub>S-(S)O<sub>3</sub> species.<sup>66</sup> The foregoing suggests that a large fraction of intermediate LiPs is mostly converted to Li<sub>2</sub>S<sub>2</sub> and Li<sub>2</sub>S at the CNTs/CNFs/Ni-Co electrode, whereas a small fraction bonds to the oxygen group on the electrode surface. In contrast, the S 2p core level of the pristine CNTs/CNFs electrode exhibited a relatively weak peak at 161.8 eV related to the low presence of Li<sub>2</sub>S<sub>2</sub> and Li<sub>2</sub>S. This was because the peak at 166.8 eV associated with the formation Li<sub>2</sub>S-(S)O<sub>3</sub> was even dominant in the spectrum. The XPS results clearly indicated that both NiCo and NiCoO<sub>2</sub> nanoparticles trigger the electrochemical reversible conversion to Li<sub>2</sub>S<sub>2</sub>/Li<sub>2</sub>S, thus acting as polysulfide mediators.<sup>64</sup> Figure 6C–D4 shows the TEM image and corresponding EDX mapping results of the CNTs/CNFs/Ni-Co electrode after the full discharge (1.8 V) at the 100th cycle. The image shows that the NiCo and NiCoO<sub>2</sub> nanoparticles are well-preserved for the cycled electrode with the

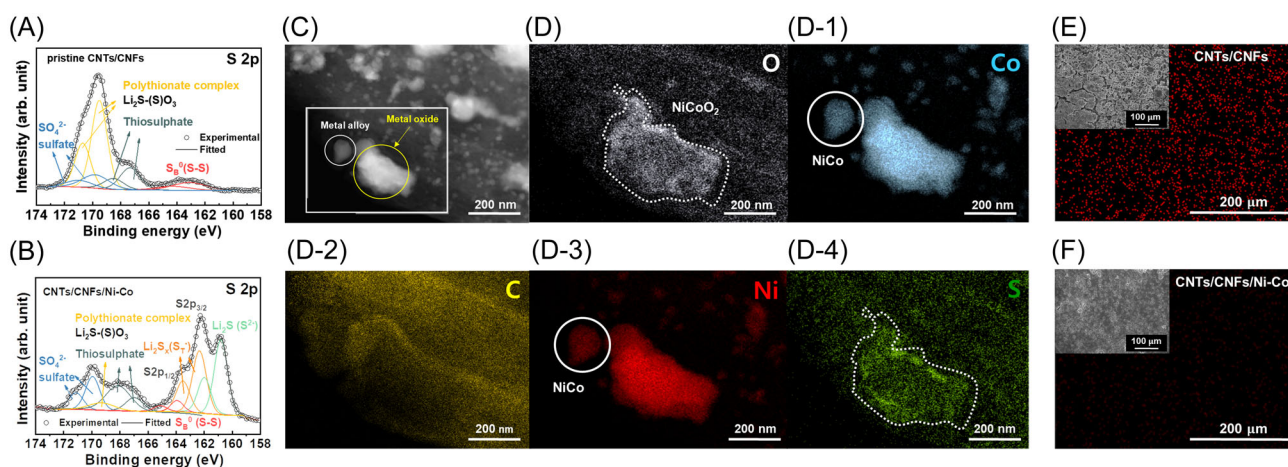
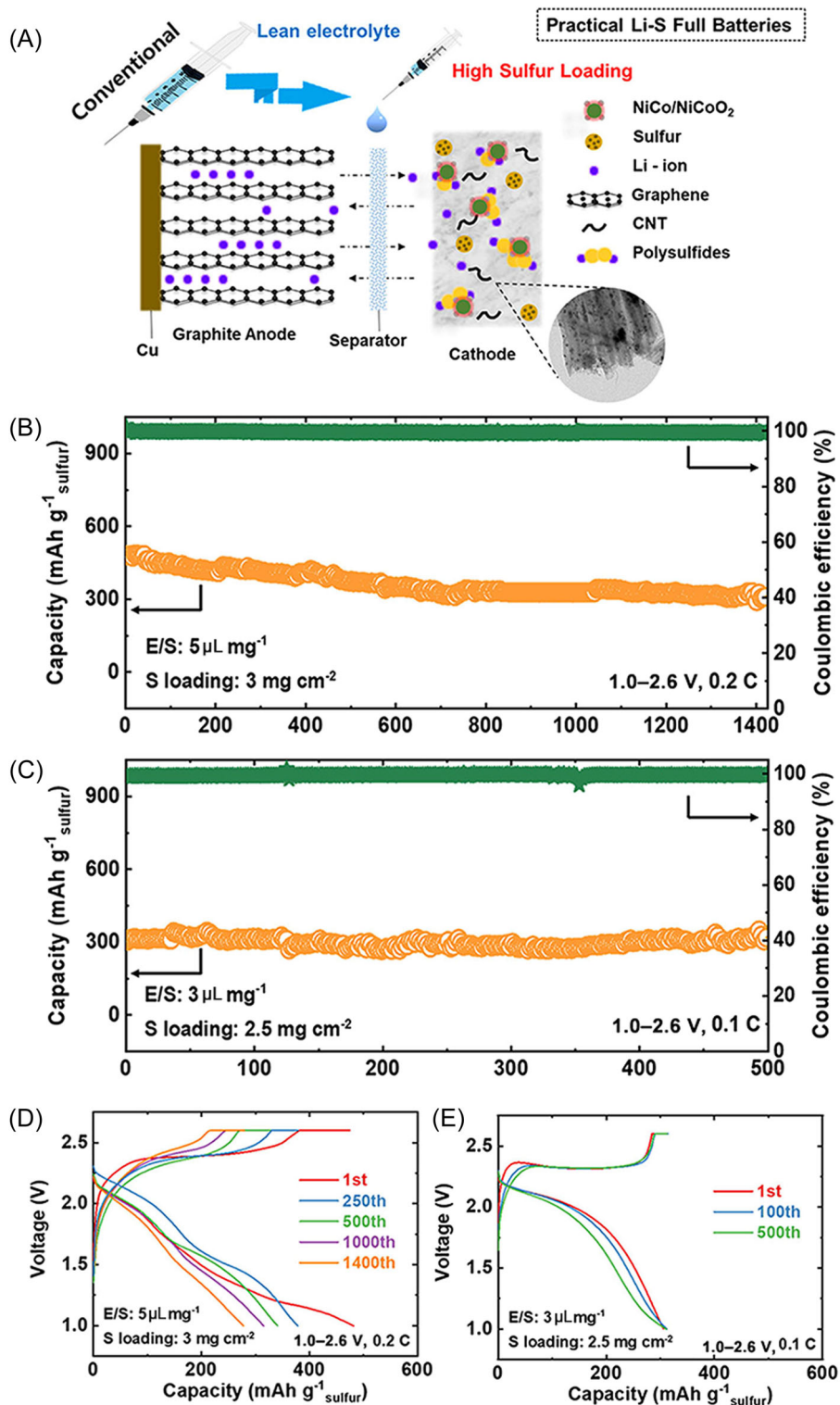


**FIGURE 6** Electrochemical mechanism of lithium/polysulfide: (A) XPS spectrum of S 2p core level corresponding to CNTs/CNFs at full discharge (1.8 V) after 100 cycles and (B) XPS spectrum of S 2p core level corresponding to CNTs/CNFs/Ni-Co at full discharge (1.8 V) after 100 cycles; (C, D) corresponding TEM–EDX mapping of CNTs/CNFs/Ni-Co at full discharge (1.8 V) after 100 cycles. SEM and elemental analysis (sulfur: red) of Li metal anodes recovered from cells using different cathodes after 100 cycles: (E) pristine CNTs/CNFs and (F) CNTs/CNFs/Ni-Co.

**FIGURE 7** (A) Schematic illustration of the proposed Li-S full battery. Long-term cycling test of the Li-S full battery with different test condition: (B) cycled at S loading:  $3 \text{ mg cm}^{-2}$ , E/S: 5, current rate:  $0.2 \text{ C}$ ; (C) cycled at S loading:  $2.5 \text{ mg cm}^{-2}$ , E/S: 3, current rate:  $0.1 \text{ C}$ . Charge-discharge voltage profiles of the Li-S full battery (D) at the 1st, 250th, 500th, 1000th, and 1400th cycle corresponding to (B) and (E) at the 1st, 100th, and 500th cycle corresponding to (C).



sulfur species enclosed and anchored to the electrode pores. A strong chemical bond is formed by NiCoO<sub>2</sub> with the LiPs based on the Lewis acid–base interactions. The better conversion reactions with chemical binding of the CNTs/CNFs/Ni–Co electrode observed in postmortem analysis showed good agreement with the DFT calculations. In addition, to better analyze the eventual LiPs migration toward the anode side, cycled Li anodes were collected from the Li/CNTs/CNFs and Li/CNTs/CNFs/Ni–Co cells after 100 cycles (discharge state at 1.8 V), and then they were analyzed through SEM–EDX mapping (Figure 6E,F). The anode recovered from the Li/CNTs/CNFs cell showed a highly faded surface due to the deposition of large amounts of sulfur on the Li metal. In contrast, the anode collected from the Li/CNTs/CNFs/Ni–Co cell exhibited a smoother surface with a considerably lower fraction of accumulated sulfur on its surface (Figure S13).

### 3.5 | Li–S full battery with lean electrolyte

The current Li–S batteries using the Li metal anode is confronted with the problem of a short lifetime and serious safety concerns, hindering their practical battery applications. To fabricate a safe and reliable Li–S battery, the use of a graphite anode is an acceptable alternative due to its low average working potential and satisfactory reversibility. Our previous work showed that an electrolyte based on 2.5 M LiTFSI + 0.4 M LiNO<sub>3</sub> dissolved in DME:DOL = 1:1 (v/v) had high compatibility because of its unique solvation chemistry with the graphite anode; hence, it was capable of delivering high reversible capacity.<sup>67,68</sup> The reversible intercalation of Li<sup>+</sup> ion into graphite with the electrolyte is indicated by the whiteness in the operando XRD analysis. The XRD patterns of the graphite anode were collected within the scanning angle (2 $\theta$ ) domain of 22–28° during the first lithiation process (Figure S14). During lithiation, the major peak at 26.3° corresponding to the (002) plane of graphite gradually shifted toward the lower scanning angle by forming the Li<sup>+</sup>–graphite intercalation compounds (GIC) of LiC<sub>12</sub>.<sup>69</sup> At the end of lithiation, the final GIC phase of the LiC<sub>6</sub> compound was clearly observed, exhibiting an identical electrochemical Li<sup>+</sup> ion intercalation reaction with the conventional electrolyte used in commercial LIBs.<sup>70</sup> The Li–S full-cell battery consisting of a lithiated-graphite anode and CNTs/CNFs/Ni–Co cathode was assembled by balancing the anode-to-cathode capacity ratio (N/P) to 1.2:1 (Figure 7A). To be competitive with commercial Li-ion batteries, the Li–S battery must operate with a lean amount of electrolyte, because a considerable portion of

the total battery weight is contributed by the electrolyte. Hence, to reasonably evaluate the practical acceptability of the proposed Li–S full-cell battery, it must be assembled with a lean amount of electrolyte.<sup>71</sup> With a high sulfur load of 3 mg cm<sup>-2</sup> and E/S of 5, the Li–S full-cell battery delivered 480.48 mAh g<sup>-1</sup> (sulfur) of high reversible capacity, showing unprecedented long-term cycling stability and high Coulombic efficiency with a current rate of 0.2 C after 1400 cycles (Figure 7B,D). Unexpectedly, the Li–S full-cell battery survives even under an extremely lean electrolyte condition (E/S of 3), demonstrating a 99.5% ultra-stable capacity retention after 500 cycles with a current rate of 0.1 C (Figure 7C,E). Although further work is necessary to achieve the practical utilization of the proposed Li–S full-cell battery, particularly in terms of increasing sulfur load (mg cm<sup>-2</sup>), the performance that has been reported in this work is superior to most of the recent state-of-the-art Li–S batteries (Table S1).

## 4 | CONCLUSION

The use of metal oxides has been reported in the state of the art of Li/S cells to alleviate sulfur dissolution and mitigate capacity fading upon cycling. Coupling oxide systems together with metal particles can also improve the electronic conductivity of sulfur-based electrodes. A new approach to the design of a practical Li–S full-cell battery with a lean amount of electrolyte is proposed. The configuration involves a unique self-standing hybrid architecture with NiCo and NiCoO<sub>2</sub> nanoparticles that are heterogeneously anchored to the CNT-embedded self-standing carbon matrix. This work demonstrates that the presence of NiCo and NiCoO<sub>2</sub> increases the interactions between the Li<sub>2</sub>S<sub>n</sub> species and electrode surface, thus substantially stabilizing the electrochemical performance. The NiCo and NiCoO<sub>2</sub> nanoparticles function as an efficient polysulfide mediator with a twofold role as follows. (1) As a polysulfide scavenger, it confines the active material (sulfur and LiPs) at the cathode side and prevents migrations to the Li anode surface under prolonged cycling. (2) As a redox-active mediator, it facilitates the electrochemical conversion reaction between Li and S, thus enhancing the electrochemical utilization of sulfur. Smart coupling of both metal and metal oxide particles shows the synergistic effect of both polysulfide anchoring and electron transfer. Furthermore, the optimized three-dimensional architecture of the CNTs/CNFs/Ni–Co electrode, the reduced free volume in between the carbon fibers after the adsorption of Li<sub>2</sub>S<sub>n</sub> species, and the high mass density of the active material all contribute to the reduction in the electrolyte volume. By employing a commercial graphite anode, this

study further demonstrated the possible use of the proposed CNTs/CNFs/Ni-Co electrode with sulfur even in a Li-S full battery configuration under a lean electrolyte condition. This shows the potential of Li-S technology in satisfying the commercial requirements of batteries with practical high energy density, long cycling, and operational safety.

## ACKNOWLEDGMENTS

This research was supported by the National Research Foundation of Korea (NRF) grant funded by the Korean government (MSIT) (NRF-2022R1C1C1011058). It was also supported by the Korea Institute for Advancement of Technology (KIAT) grant funded by the Korean Government (MOTIE) (P0012748, HRD Program for Industrial Innovation).

## CONFLICT OF INTEREST STATEMENT

The authors declare that there are no conflicts of interests.

## ORCID

Jongsoo Kim  <http://orcid.org/0000-0002-7651-5516>  
 Yang-Kook Sun  <http://orcid.org/0000-0002-0117-0170>  
 Jang-Yeon Hwang  <http://orcid.org/0000-0003-3802-7439>

## REFERENCES

- Mosavati N, Salley SO, Ng KYS. Characterization and electrochemical activities of nanostructured transition metal nitrides as cathode materials for lithium sulfur batteries. *J Power Sources*. 2017;340(1):210-216.
- Nitta N, Wu F, Lee JT, Yushin G. Li-ion battery materials: present and future. *Mater Today*. 2015;18(5):252-264.
- Chu S, Cui Y, Liu N. The path towards sustainable energy. *Nat Mater*. 2016;16(1):16-22.
- Scrosati B, Hassoun J, Sun Y-K. Lithium-ion batteries. A look into the future. *Energy Environ Sci*. 2011;4(9):3287-3295.
- Tarascon J-M, Armand M. Issues and challenges facing rechargeable lithium batteries. *Nature*. 2001;414(6861):359-367.
- Choi JW, Aurbach D. Promise and reality of post-lithium-ion batteries with high energy densities. *Nat Rev Mater*. 2016;1(4):16013.
- Wu F, Yushin G. Conversion cathodes for rechargeable lithium and lithium-ion batteries. *Energy Environ Sci*. 2017;10(2):435-459.
- Yang Y, Yu G, Cha JJ, et al. Improving the performance of lithium-sulfur batteries by conductive polymer coating. *ACS Nano*. 2011;5(11):9187-9193.
- Agostini M, Matic A. Designing highly conductive functional groups improving guest-host interactions in Li/S batteries. *Small*. 2020;16(2):1905585.
- Manthiram A, Fu Y, Chung S-H, Zu C, Su Y-S. Rechargeable lithium-sulfur batteries. *Chem Rev*. 2014;114(23):11751-11787.
- Seh ZW, Sun Y, Zhang Q, Cui Y. Designing high-energy lithium-sulfur batteries. *Chem Soc Rev*. 2016;45(20):5605-5634.
- Ji X, Lee KT, Nazar LF. A highly ordered nanostructured carbon-sulphur cathode for lithium-sulphur batteries. *Nat Mater*. 2009;8(6):500-506.
- Bresser D, Passerini S, Scrosati B. Recent progress and remaining challenges in sulfur-based lithium secondary batteries—a review. *Chem Commun*. 2013;49(90):10545-10562.
- Agostini M, Xiong S, Matic A, Hassoun J. Polysulfide-containing glyme-based electrolytes for lithium sulfur battery. *Chem Mater*. 2015;27(13):4604-4611.
- Agostini M, Sadd M, Xiong S, et al. Designing a safe electrolyte enabling long-life Li/S batteries. *ChemSusChem*. 2019;12(18):4176-4184.
- Hwang J-Y, Kim HM, Shin S, Sun Y-K. Designing a high-performance lithium-sulfur batteries based on layered double hydroxides-carbon nanotubes composite cathode and a dual-functional graphene-polypropylene-Al<sub>2</sub>O<sub>3</sub> separator. *Adv Funct Mater*. 2018;28(3):1704294.
- Li M, Wan Y, Huang J-K, et al. Metal-organic framework-based separators for enhancing Li-S battery stability: mechanism of mitigating polysulfide diffusion. *ACS Energy Lett*. 2017;2(10):2362-2367.
- Ji X, Lee KT, Nazar LF. A highly ordered nanostructured carbon-sulphur cathode for lithium-sulphur batteries. *Nat Mater*. 2009;8(6):500-506.
- Jayaprakash N, Shen J, Moganty SS, Corona A, Archer LA. Porous hollow carbon@sulfur composites for high-power lithium-sulfur batteries. *Angew Chem Int Ed*. 2011;50(26):5904-5908.
- Wang W, Cao Z, Elia GA, et al. Recognizing the mechanism of sulfurized polyacrylonitrile cathode materials for Li-S batteries and beyond in Al-S batteries. *ACS Energy Lett*. 2018;3(12):2899-2907.
- Kumar R, Liu J, Hwang J-Y, Sun Y-K. Recent research trends in Li-S batteries. *J Mater Chem A*. 2018;6(25):11582-11605.
- Wahyudi W, Cao Z, Kumar P, et al. Phase inversion strategy to flexible freestanding electrode: critical coupling of binders and electrolytes for high performance Li-S battery. *Adv Funct Mater*. 2018;28(34):1802244.
- Agostini M, Hwang J-Y, Kim HM, et al. Minimizing the electrolyte volume in Li-S batteries: A step forward to high gravimetric energy density. *Adv Energy Mater*. 2018;8(26):1801560.
- Pang Q, Liang X, Kwok CY, Nazar LF. Advances in lithium-sulfur batteries based on multifunctional cathodes and electrolytes. *Nat Energy*. 2016;1(9):16132.
- Sun Y-K, Yoon CS. Growing instead of confining. *Nat Energy*. 2017;2(10):768-769.
- Pan H, Chen J, Cao R, et al. Non-encapsulation approach for high-performance Li-S batteries through controlled nucleation and growth. *Nat Energy*. 2017;2(10):813-820.
- Xiang Y, Lu L, Kottapalli AGP, Pei Y. Status and perspectives of hierarchical porous carbon materials in terms of high-performance lithium-sulfur batteries. *Carbon Energy*. 2022;4(3):346-398.
- Fretz SJ, Agostini M, Jankowski P, Johansson P, Matic A, Palmqvist AEC. Amine- and amide-functionalized mesoporous carbons: a strategy for improving sulfur/host interactions in Li-S batteries. *Batter Supercaps*. 2020;3(8):757-765.
- Sun J, Hwang J-Y, Jankowski P, et al. Critical role of functional groups containing N, S, and O on graphene surface for stable and fast charging Li-S batteries. *Small*. 2021;17(17):2007242.

30. Wang X-R, Liu J-Y, Liu Z-W, et al. Identifying the key role of pyridinic-N-Co bonding in synergistic electrocatalysis for reversible ORR/OER. *Adv Mater.* 2018;30(23):1800005.
31. Hao S, Chen L, Yu C, et al. NiCoMo hydroxide nanosheet arrays synthesized via chloride corrosion for overall water splitting. *ACS Energy Lett.* 2019;4(4):952-959.
32. Li J, Li Y, Xue Q, Gao Y, Ma Y. Phytate-coordination triggered enrichment of surface NiOOH species on nickel foam for efficient urea electrooxidation. *Chin J Struct Chem.* 2022;41(7):2207035-2207039.
33. Li J, Liu H-X, Gou W, et al. Ethylene-glycol ligand environment facilitates highly efficient hydrogen evolution of Pt/CoP through proton concentration and hydrogen spillover. *Energy Environ Sci.* 2019;12(7):2298-2304.
34. Liang X, Kwok CY, Lodi-Marzano F, et al. Tuning transition metal oxide-sulfur interactions for long life lithium sulfur batteries: the "goldilocks" principle. *Adv Energy Mater.* 2016;6(6):1501636.
35. Marangon V, Scaduti E, Vinci VF, Hassoun J. Scalable composites benefiting from transition-metal oxides as cathode materials for efficient lithium-sulfur batteries. *ChemElectroChem.* 2022;9(11):e202200374.
36. Hwang J-Y, Kim HM, Lee S-K, et al. High-energy, high-rate, lithium-sulfur batteries: synergetic effect of hollow TiO<sub>2</sub>-webbed carbon nanotubes and a dual functional carbon-paper interlayer. *Adv Energy Mater.* 2016;6(1):1501480.
37. Yao H, Zheng G, Hsu PC, et al. Improving lithium-sulphur batteries through spatial control of sulphur species deposition on a hybrid electrode surface. *Nat Commun.* 2014;5:3943.
38. Wang J, Zhou L, Guo D, et al. Flower-like NiS<sub>2</sub>/WS<sub>2</sub> heterojunction as polysulfide/sulfide bidirectional catalytic layer for high-performance lithium-sulfur batteries. *Small.* 2023;19(11):2206926.
39. Yang B, Guo D, Lin P, et al. Hydroxylated multi-walled carbon nanotubes covalently modified with tris(hydroxypropyl) phosphine as a functional interlayer for advanced lithium-sulfur batteries. *Angew Chem Int Ed.* 2022;61(28):202204327.
40. Dai YY, Xu CM, Liu XH, et al. Manipulating metal-sulfur interactions for achieving high-performance S cathodes for room temperature Li/Na-sulfur batteries. *Carbon Energy.* 2021;3(2):253-270.
41. Wang Z, Yan Y, Zhang Y, et al. Single-atomic Co-B<sub>2</sub>N<sub>2</sub> sites anchored on carbon nanotube arrays promote lithium polysulfide conversion in lithium-sulfur batteries. *Carbon Energy.* 2023;5(11):e306.
42. Kresse G, Furthmüller J. Efficiency of ab-initio total energy calculations for metals and semiconductors using a plane-wave basis set. *Comput Mater Sci.* 1996;6(1):15-50.
43. Blöchl PE. Projector augmented-wave method. *Phys Rev B.* 1994;50(24):17953-17979.
44. Perdew JP, Burke K, Ernzerhof M. Generalized gradient approximation made simple. *Phys Rev Lett.* 1996;77(18):3865-3868.
45. Anisimov VI, Aryasetiawan F, Lichtenstein AI. First-principles calculations of the electronic structure and spectra of strongly correlated systems: the LDA + U method. *J Phys Condens Matter.* 1997;9(4):767-808.
46. Jiang J, Sun F, Zhou S, et al. Atomic-level insight into super-efficient electrocatalytic oxygen evolution on iron and vanadium co-doped nickel (oxy)hydroxide. *Nat Commun.* 2018;9:2885.
47. Nawa K, Miura Y. Exploring half-metallic Co-based full Heusler alloys using a DFT+U method combined with linear response approach. *RSC Adv.* 2019;9(52):30462-30478.
48. Grimme S, Antony J, Ehrlich S, Krieg H. A consistent and accurate ab initio parametrization of density functional dispersion correction (DFT-D) for the 94 elements H-Pu. *J Chem Phys.* 2010;132(15):154104.
49. Chen R, Hu Y, Shen Z, et al. Facile fabrication of foldable electrospun polyacrylonitrile-based carbon nanofibers for flexible lithium-ion batteries. *J Mater Chem A.* 2017;5(25):12914-12921.
50. Sheen Mers SV, Ganesh V. Binary metallic sponges as an efficient electrocatalyst for alkaline water electrolysis. *SN Appl Sci.* 2020;2(7):1149.
51. Li Y, Peng H, Yang L, Dong H, Xiao P. Investigating the effect of sulfur and selenium on the electrochemical properties of nickel-cobalt oxides: enhanced charge capacity and composition-property relationships. *J Mater Sci.* 2016;51(15):7108-7118.
52. Biesinger MC, Payne BP, Grosvenor AP, W.M. Lau LWM, Gerson AR, S.C. Smart RSC. Resolving surface chemical states in XPS analysis of first row transition metals, oxides and hydroxides: Cr, Mn, Fe, Co and Ni. *Appl Surf Sci.* 2011;257(7):2717-2730.
53. Xu H, Shi Z-X, Tong Y-X, Li G-R. Porous microrod arrays constructed by carbon-confined NiCo@NiCoO<sub>2</sub> core@Shell nanoparticles as efficient electrocatalysts for oxygen evolution. *Adv Mater.* 2018;30(21):1705442.
54. Fu Y, Yu H-Y, Jiang C, et al. NiCo alloy nanoparticles decorated on N-doped carbon nanofibers as highly active and durable oxygen electrocatalyst. *Adv Funct Mater.* 2018;28(9):1705094.
55. Liu X, Park M, Kim MG, Gupta S, Wu G, Cho J. Integrating NiCo alloys with their oxides as efficient bifunctional cathode catalysts for rechargeable zinc-air batteries. *Angew Chem Int Ed.* 2015;54(33):9654-9658.
56. Woo J-Y, Kim A-Y, Kim MK, et al. Cu<sub>3</sub>Si-doped porous-silicon particles prepared by simplified chemical vapor deposition method as anode material for high-rate and long-cycle lithium-ion batteries. *J Alloys Compd.* 2017;701(1):425-432.
57. Kulkarni AK, Schulz KH, Lim TS, Khan M. Dependence of the sheet resistance of indium-tin-oxide thin films on grain size and grain orientation determined from X-ray diffraction techniques. *Thin Solid Films.* 1999;345(2):273-277.
58. Wang H, Zhang W, Xu J, Guo Z. Advances in polar materials for lithium-sulfur batteries. *Adv Funct Mater.* 2018;28(38):1707520.
59. Wang Y, Zhao Y, Liu K, et al. Li intercalation in an MoSe<sub>2</sub> electrocatalyst: in situ observation and modulation of its precisely controllable phase engineering for a high-performance flexible Li-S battery. *Carbon Energy.* 2023;5(2):e255.
60. Zou Q, Lu Y-C. Solvent-dictated lithium sulfur redox reactions: an operando UV-vis spectroscopic study. *J Phys Chem Lett.* 2016;7(8):1518-1525.
61. Balach J, Linnemann J, Jaumann T, Giebeler L. Metal-based nanostructured materials for advanced lithium-sulfur batteries. *J Mater Chem A.* 2018;6(46):23127-23168.
62. Tang X, Xu Z, Sun Z, et al. Factors of kinetics processes in lithium-sulfur reactions. *Energy Technol.* 2019;7(12):1900574.

63. Zhang B-W, Sheng T, Liu Y-D, et al. Atomic cobalt as an efficient electrocatalyst in sulfur cathodes for superior room-temperature sodium-sulfur batteries. *Nat Commun.* 2018;9:4082.
64. Kim HM, Hwang J-Y, Bang S, et al. Tungsten oxide/zirconia as a functional polysulfide mediator for high-performance lithium-sulfur batteries. *ACS Energy Lett.* 2020;5(10):3168-3175.
65. Hou Y, Qiu M, Kim MG, et al. Atomically dispersed nickel-nitrogen-sulfur species anchored on porous carbon nanosheets for efficient water oxidation. *Nat Commun.* 2019;10:1392.
66. Cai D, Lu M, Li L, et al. A highly conductive MOF of graphene analogue  $\text{Ni}_3(\text{HITP})_2$  as a sulfur host for high-performance lithium-sulfur batteries. *Small.* 2019;15(44):1902605.
67. Hwang J-Y, Shin S, Yoon CS, Sun Y-K. Nano-compacted  $\text{Li}_2\text{S}$ /graphene composite cathode for high-energy lithium-sulfur batteries. *ACS Energy Lett.* 2019;4(12):2787-2795.
68. Ming J, Cao Z, Wahyudi W, et al. New insights on graphite anode stability in rechargeable batteries: Li ion coordination structures prevail over solid electrolyte interphases. *ACS Energy Lett.* 2018;3(2):335-340.
69. Jiang Z, Alamgir M, Abraham KM. The electrochemical intercalation of Li into graphite in Li/polymer electrolyte/graphite cells. *J Electrochem Soc.* 1995;142(2):333-340.
70. Megahed S, Scrosati B. Lithium-ion rechargeable batteries. *J Power Sources.* 1994;51(1-2):79-104.
71. Yang B, Wang J, Qi Y, et al. Strong internal electric field enhanced polysulfide trapping and ameliorates redox kinetics for lithium-sulfur battery. *J Energy Chem.* 2023;77:376-383.

## SUPPORTING INFORMATION

Additional supporting information can be found online in the Supporting Information section at the end of this article.

**How to cite this article:** Park H, Lee S, Kim H, et al. Heterostructured nickel-cobalt metal alloy and metal oxide nanoparticles as a polysulfide mediator for stable lithium-sulfur full batteries with lean electrolyte. *Carbon Energy.* 2024;6:e472. doi:10.1002/cey2.472